Imaging with high resolution and wide field of view based on an ultrathin microlens array

Xueqian Wang,[1] Chuanbao Liu,[2] Lijie Qiao,[1] Ji Zhou,[3] Yang Bai,[1,*] and Jingbo Sun[3,†]

[1] *Beijing Advanced Innovation Center for Materials Genome Engineering, Institute for Advanced Materials and Technology, University of Science and Technology Beijing, Beijing 100083, China*

[2] *School of Materials and Engineering, University of Science and Technology Beijing, Beijing 100083, China*

[3] *State Key Laboratory of New Ceramics and Fine Processing, School of Materials Science and Engineering, Tsinghua University, Beijing 100084, China*

(Received 9 November 2023; revised 14 February 2024; accepted 26 February 2024; published 19 March 2024)

An outstanding challenge for micro-optical systems is to achieve high resolution under wide-field-of-view (FOV) imaging. We propose a compact solution for high-resolution imaging under a wide-FOV with wavelength-scale thickness achromatic microlens arrays. Our strategy involves using aspherical sublenses to reduce spherical and chromatic aberration, as well as using small-diameter achromatic microlenses to decrease incident ray height. With the aid of computational reconstruction, the array of microlenses can achieve a wide-FOV comparable to that of commercially available lenses with equivalent large diameters. The microlens array shows a significant advantage in imaging resolution and an order smaller thickness compared to commercial lenses. This highly integrated microlens array, characterizing high-resolution imaging under a wide-FOV, will play an important role in applications such as autonomous driving, endoscopy, virtual reality, and augmented reality.

DOI: 10.1103/PhysRevApplied.21.034035

I. INTRODUCTION

For highly integrated optical applications, such as light detection and ranging, biomedical endoscopy, and head-mounted augmented reality devices, smaller imaging systems with high resolution and wide field of view (FOV) are always highly desired. The emergence of metalenses offers a new opportunity for high-performance miniaturized optics with small size and light weight [1–4]. Metalenses consist of a dense arrangement of subwavelength scatterers in an ultrathin interface that allows a flexible modulation of the wave front of the optical field. They focus light into a diffraction-limited focal point, so large FOV designs based on metalenses are widely studied [5–9]. Firstly, metalenses with wide-angle phases are prepared for imaging relatively large areas at short object distances [10–14]. Although a considerable FOV can be obtained, the use of a wide-angle phase introduces off-axis aberration, resulting in a severe distortion at the image edges. This aberration can be corrected by metalens doublets, but this comes at the cost of higher manufacturing complexity [15–18]. Furthermore, based on the properties of the planar optics of metalenses, increasing their size does not induce additional spherical aberration. Consequently, some researchers have developed large-diameter metalenses to achieve a wide FOV [19–22]. However, the use of larger focal lengths leads to an inevitable increase in working distance and overall system size, which undermines the benefits of the compact and slim nature of metalenses. In order to achieve a wide FOV while maintaining a compact system, researchers have explored the arrangement of multiple metalenses into arrays [23–26]. However, these arrays are typically designed for specific wavelengths or polarization states, imposing constraints on the incident light and making it difficult to correct for wideband chromatic aberrations. To overcome this limitation, additional procedures such as distortion correction and background subtraction are required to generate the final image [5]. Additionally, the presence of a large number of unit cell structures not only leads to discontinuities in the phase profile and deviations in the response of the structural units from the ideal values, resulting in low efficiency, but also presents challenges in terms of the fabrication techniques and computational resources required for metalens simulation [27–29].

Microlenses can achieve thicknesses on the wavelength scale that are comparable to metalenses, while also producing near diffraction-limited focal spots [30–32]. Their straightforward and continuous design allows for efficient focusing and a simpler manufacturing process [33–35].

*baiy@mater.ustb.edu.cn
†jingbosun@mail.tsinghua.edu.cn

However, the issue with traditional microlenses is that larger diameters inevitably result in thicker lenses, leading to increased spherical aberration and a decrease in the resolution of wide-field imaging. Here, we present an achromatic microlens array for high-resolution wide-field imaging. Each sublens is an aspherical microlens with a thickness on the order of the wavelength, allowing for achromatic focusing near the diffraction limit. The design employs smaller diameters to reduce the relative height of incident light rays, thus minimizing spherical aberration. Through an expandable format, this array maintains a wide-FOV comparable to that of larger diameter lenses. Our achromatic microlens array features an ultrathin thickness of 1.12 μm and numerical aperture (NA) of 0.178, which enables a FOV of about 288×206 μm^2 and a high resolution of 2.25 μm under white light imaging. In comparison to commercially available lenses with an equivalent large diameter and similar FOV and NA (thickness of 18.37 μm, NA of 0.161, and FOV of 280×200 μm^2), our imaging system demonstrates a significant improvement in resolution while reducing the thickness by an order of magnitude.

II. DESIGN OF BROADBAND ACHROMATIC ASPHERICAL MICROLENSES

To focus on a diffraction-limited spot with an aspherical profile, the phase provided by the thickness profile needs to satisfy [30]

$$k(n-1)(d-d_0) = -k\left(\sqrt{r^2+f^2}-f\right), \qquad (1)$$

where k, r, d, and f represent wave vector, radial coordinate, lens thickness at each position r, and focal length of the lens, respectively. d_0 is the thickness at the center of the lens, which is the maximum value of d, and n is the refractive index. Since transparent materials conform to the Cauchy model, n decreases as the wavelength increases in the visible region. So, the design wavelength is selected as the smallest wavelength of 400 nm in the visible range. This wavelength corresponds to the largest refractive index in the visible range, yielding the thinnest lens configuration. For a microlens with radius r_0, Eq. (1) can be expressed as

$$f = \frac{r_0^2 - d_0^2(n-1)^2}{2(n-1)d_0}. \qquad (2)$$

In practice, there is dispersion in the lens material. The theoretical focal length of a curved microlens exhibits a monotonic relationship with wavelength. The degree of chromatic aberration in the microlens can be described using absolute and relative chromatic aberrations [36]. Absolute chromatic aberration ($|df|$) is defined as the difference in focal length between the maximum and minimum wavelengths. Relative chromatic aberration, also known as focal length shift (S), is expressed as the ratio of $|df|$ to the average focal length within the operating bandwidth. According to Eq. (2), the formulas for $|df|$ and S can be expressed as follows:

$$|df| = \left|\frac{-r_0^2}{2(n-1)^2 d_0} - \frac{d_0}{2}\right| dn, \qquad (3)$$

$$S = \frac{|df|}{f} = \frac{|\Delta n[d_0^2(n-1)^2 + r_0^2]|}{[r_0^2 - d_0^2(n-1)^2](n-1)}, \qquad (4)$$

where Δn represents the difference in refractive index between the minimum and maximum wavelengths. According to reported literature [36,37], when S is not greater than 10%, it can be considered as achromatic focusing, and $|df|$ should not exceed $f \times S$. According to Eqs. (3) and (4), the achromatic lens should be made of a low-dispersion material to suppress chromatic aberration. We selected S1813 positive photoresist with low dispersion. The refractive index of S1813 photoresist was measured using an ellipsometer (VASE Ellipsometer) at visible light wavelengths. The refractive indices at 400 and 700 nm are 1.710 and 1.647, respectively, resulting in Δn of 0.063. The microlens was designed with a diameter of 18 μm, a central thickness of 1.12 μm, and a focal length of 50.5 μm. The values of $|df|$ and S are calculated as 4.48 μm and 9%, respectively, satisfying the requirements for chromatic aberration correction. According to Eq. (1), the lens profile adheres to the equation

$$d = d_0 - \frac{\sqrt{r^2+f^2}-f}{n-1}. \qquad (5)$$

The distribution of the ideal thickness profile of the lens is shown as the red line in Fig. 1(b). We performed numerical simulations of the designed lens using the COMSOL Multiphysics commercial software package. The simulation method and results are detailed in Sec. I of the Supplemental Material [41]. The results are basically consistent with the theoretical calculations, showing diffraction-limited spots and an average focal length of 52 μm.

III. CHARACTERISTICS OF BROADBAND ACHROMATIC MICROLENSES

We fabricated the single microlens through laser direct writing; the detailed fabrication process is described in Sec. II of the Supplemental Material [41]. The regular circular outer contour was imaged by a scanning electron microscope (SEM), as shown in Fig. 1(a). We further characterized the thickness profile by atomic force microscopy (AFM), shown as the blue line in Fig. 1(b). The diameter of the microlens is 18 μm, and the center thickness

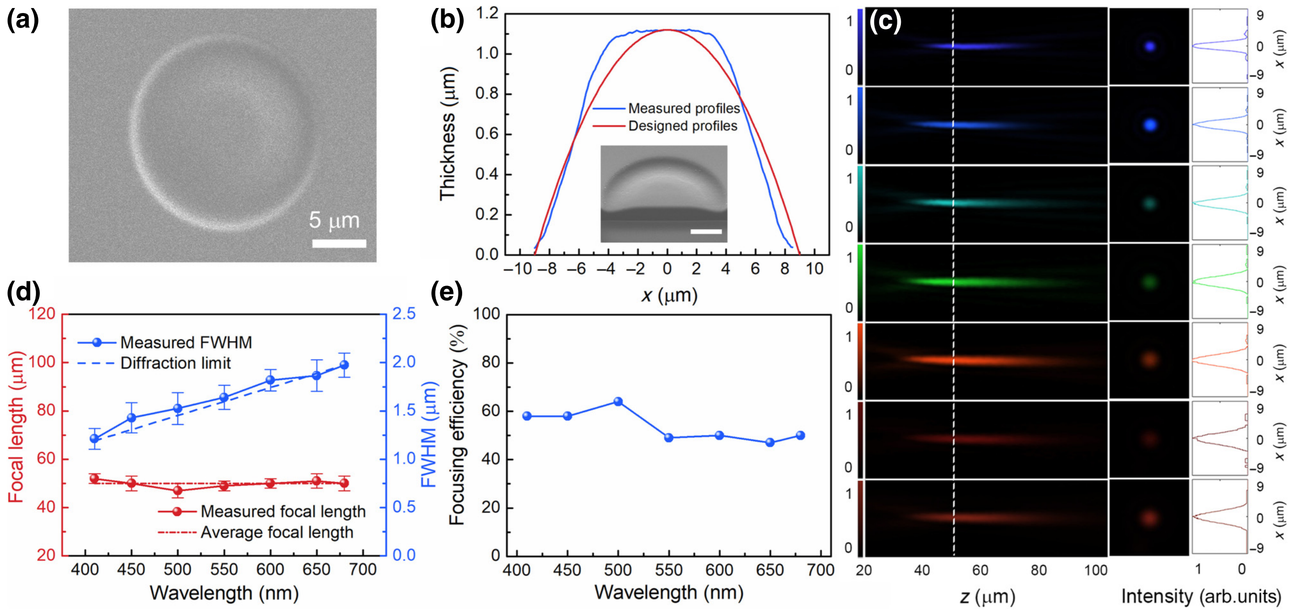

FIG. 1. (a) SEM image of the fabricated microlens with a diameter of 18 μm. (b) The thickness profile measured by AFM and the designed profile calculated by Eq. (5). The inset is a cross section of the microlens cut through the center at a 45° angle of view. Scale bar: 5 μm. (c) Normalized intensity distribution in the *x*-*z* plane of the fabricated achromatic microlens at different wavelengths from 410 to 680 nm. The white dashed line represents the average focal length of 50 μm. The right-hand panel represents the focal spots and the PSFs. (d) Measured focal lengths and FWHMs of the achromatic microlens. The red dashed line represents the average focal length of 50 μm and the blue dashed line represents the diffraction limit at various wavelengths, respectively. (e) Measured focusing efficiency of the achromatic microlens.

is 1.12 μm as designed. It is worth noting that the contour of the fabricated lens top is flatter than the design, which is drawn in red. We performed simulations comparing the designed lenses with actual measured surfaces. As discussed in Sec. III of the Supplemental Material [41], the results show a very little difference between the two microlenses. The focal length, full width at half maximum (FWHM), and focusing ability are only slightly reduced, and the resolution is slightly increased. This has a negligible effect on imaging. The experimental focusing behavior of a single microlens is measured using the customized optical setup as shown in Fig. S4(a) in the Supplemental Material [41]. Figure 1(c) shows the measured intensity distribution of an achromatic microlens at different wavelengths in the *x*-*z* plane. For the broadband wavelength region ranging from 410 to 680 nm, the focal spots are all distributed around the designed position (average focal length of 50 μm, which is marked by white dashed line). The *z* values of maximum intensity at each wavelength are extracted as focal lengths, which are depicted in Fig. 1(d). The microlens exhibits a $|df|$ of 3.5 μm and S of 7% over the entire operating bandwidth, which means achromatic focusing can be realized.

The intensity distribution of the focal plane and the point spread function (PSF) are presented in the right panel of Fig. 1(c). The focal spots are close to the ideal Airy disk with no significant distortion. Then we measured the FWHM of the focal spots for all wavelengths, and the results are plotted in Fig. 1(d). This shows that all the focal spots are near the diffraction limit (approximately $\lambda/2\mathrm{NA}$). The measured efficiency of the microlens is defined as the focal spot power divided by the transmitted power through an aperture of the same diameter as the microlens. The focal spot size is defined as 3 times the FWHM for the purpose of measuring the efficiency [38]. As depicted in Fig. 1(e), the microlens demonstrates an impressive average efficiency of 55%. This high efficiency can be attributed to its continuous and smooth surface profile, which avoids additional scattering and resonance losses. The smooth thickness profile also contributes to the microlens having a propagation phase that closely matches the desired hyperbolic phase, resulting in the absence of secondary focal spots. Consequently, the focal spot exhibits a higher intensity, leading to enhanced efficiency. This represents a favorable advancement compared to recent achromatic metalenses [39].

IV. THE MICROLENS ARRAY WITH HIGH RESOLUTION AND WIDE-FOV IMAGING

We fabricated a lens array consisting of 50 × 50 achromatic microlenses, and the optical images are shown in Figs. 2(a) and 2(b). These images clearly demonstrate the precise fabrication technique used, as the microlens

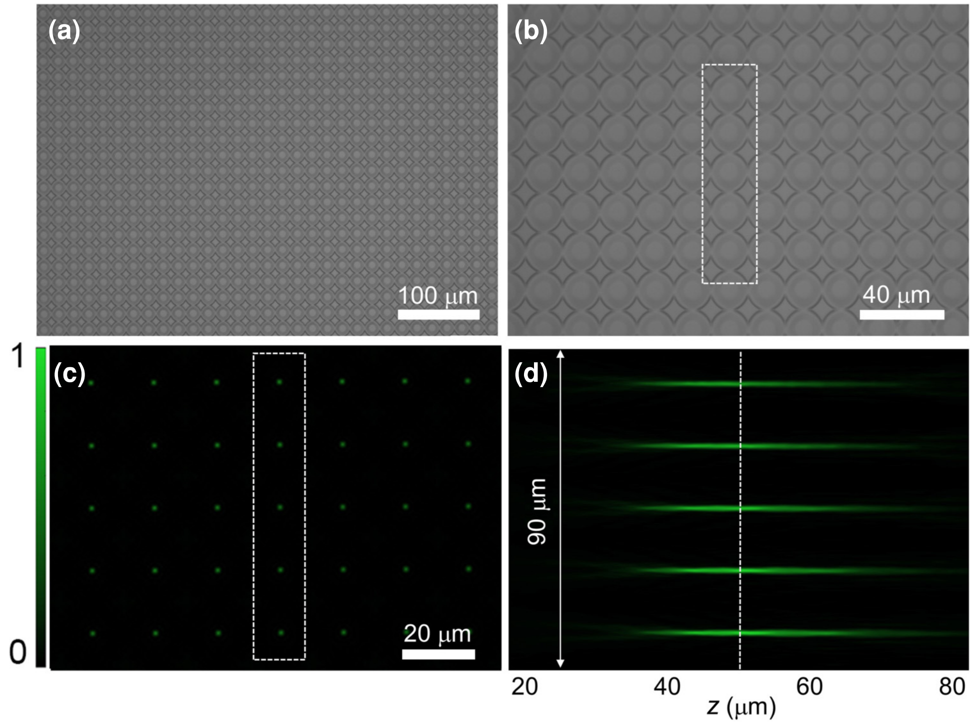

FIG. 2. (a) Optical image of the fabricated achromatic microlens array; the diameter of each sublens is 18 μm. (b) Enlarged image of a portion of the microlens array shown in (a) with a larger magnification. (c) The distribution of light intensity in the focal plane under 550-nm incident light. (d) Intensity distributions in the x-z plane, corresponding to the five sublenses highlighted in the white dashed box in (b),(c). The dashed line represents the focal length of 50 μm derived from the intensity peak of each sublens.

arrays exhibit well-defined and uniform structures. The light intensity profile after the incident beam had passed through the microlens arrays was experimentally tested. The focal plane of the lens array was specifically examined at an incident light wavelength of 550 nm, as depicted in Fig. 2(c). Remarkably, the focal plane image showcases the individual sublenses focusing effectively in their respective regions, indicating the absence of any diffraction interference or distortion. Figure 2(d) shows the x-z plane measured light intensity distributions of the lenses marked by dotted lines in Figs. 2(b) and 2(c). It is evident that each sublens exhibits uniform and precise focusing characteristics, featuring a focal length of 50 μm and a distinct bright focus. Additionally, we conducted tests to assess the broadband achromatic focusing capabilities of the lens array across a wavelength range of 410 to 680 nm. As an example, we extracted the light intensity distribution of the sublens located in the center of the dashed box from the array-modulated light field. This selection serves as a demonstration of the lens array's ability to achieve achromatic focusing over a wide range of wavelengths. Figure 3(a) presents the focal lengths of the microlenses at different wavelengths, and it is apparent that they are consistently distributed around 50 μm. This remarkable achromatic behavior indicates the lens array's excellent performance across a broad range of wavelengths.

For a more comprehensive performance comparison between single lenses and sublenses within the array, we assessed their focal lengths and FWHMs, as demonstrated in Figs. 3(b) and 3(c). The focal lengths of the two types of lenses are nearly identical, showcasing nearly diffraction-limited focusing capabilities. Moreover, the interference resulting from the periodic arrangement of the microlenses is negligible. This is an important finding, as it guarantees reliable and high-quality performance for wide-field imaging in multi-optical-axis systems.

Subsequently, we conducted a wide-field imaging test using an achromatic microlens array. In this test, we employed the 1951 United States Air Force (USAF) resolution test chart (Thorlabs, R3L3S1N) as the target object and illuminated it with white light from halogen lamps. The experimental setup utilized for imaging and additional details are provided in Fig. S4(b) of the Supplemental Material [41]. The microlens array forms various subimages on the sensing plane with the information collected by the sublenses. The relationship between the position of the microlens array and the sensing plane as well as the objective image plane follows the Gaussian lens equation,

$$\frac{1}{u}+\frac{1}{v}=\frac{1}{f_{\text{microlens}}}, \tag{6}$$

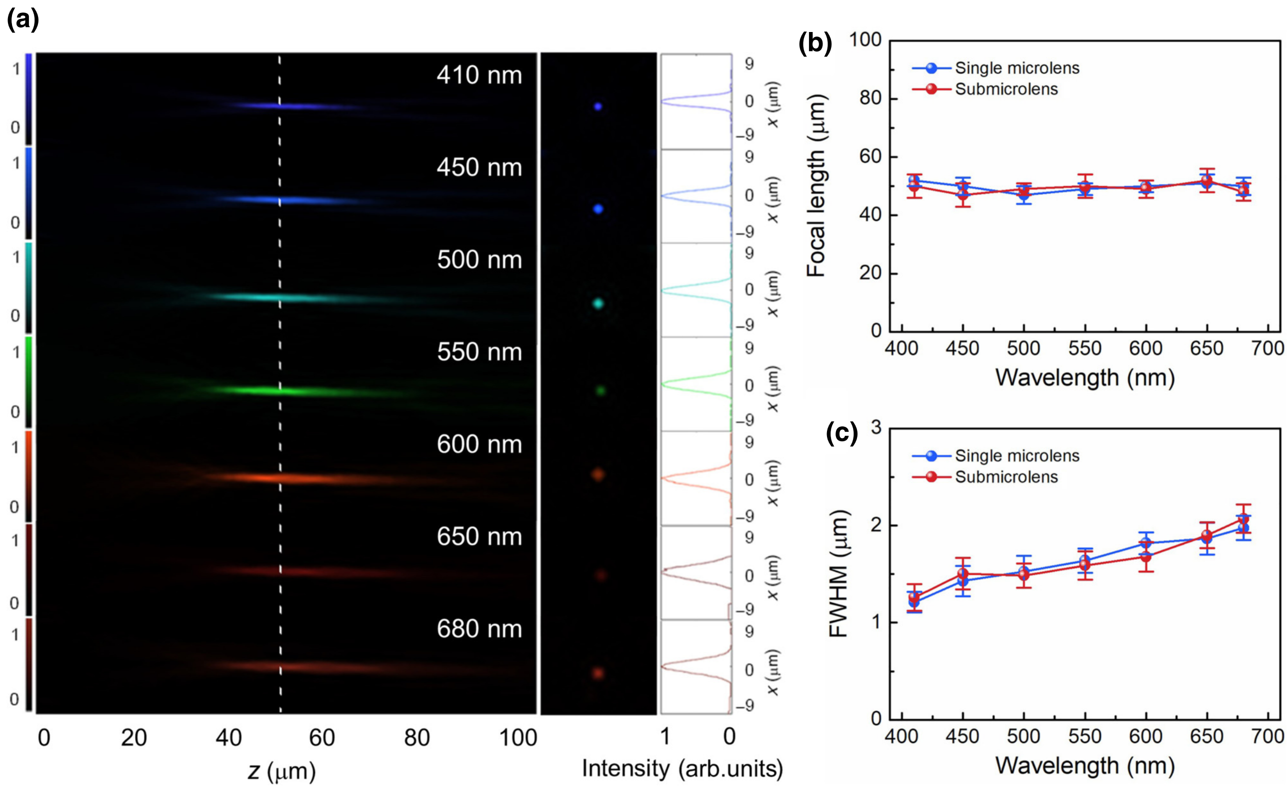

FIG. 3. (a) The normalized intensity distribution in the x-z plane for the sublens located at the center of the dashed box in Fig. 2(b) at various wavelengths (410–680 nm); the white dashed line represents the average focal length of 50 μm. The right-hand panels represent the focal plane intensity distributions and PSFs. The comparison between single lens and sublens in the array for (b) focal length and (c) FWHM.

where u, v, and $f_{\text{microlens}}$ represent the distance from the objective image plane to the lens array, the distance from the lens array to the sensing plane, and the focal length of the sublens in the array, respectively. Owing to the limited number of pixels on the charge-coupled device image sensor (2748×3840, MER-1070-14U3C-L), the actual number of lenses performing effective work in the lens array is about 10×15. The resolution target image is shown in Fig. S5(a) in the Supplemental Material [41], and the raw light field image of the resolution target image formed by the lens array is shown in Fig. S5(b) in the Supplemental Material [41]. The light field image consists of about 10×15 complete subimages, with a single subimage containing 249 pixels. Imaging shows a wide-FOV of 288×206 μm^2, which is 150 times the imaging area of a single microlens, and the resolution is not sacrificed. The quality of each subimage is clear and easily distinguishable, making them suitable for image block rendering and stitching. The rendering methods are described in Fig. S4(c) of Sec. IV of the Supplemental Material [41]. The image obtained from our experiment is shown in Fig. 4(a), and the smallest line that can be distinguished with clarity is 2.25 μm in group 5-2. This value is close to the Rayleigh criterion (0.61λ/NA) for different wavelengths. However, it should be noted that there is a slight checkerboard effect artifact, which is a blurry characteristic of the reconstructed image produced by the microlens array [8]. This blur can be attributed to differences in brightness between the sublens images, as well as factors such as noise, experimental error, and other sources of variation. Furthermore, we prepared a Ag film patterned with the letters USTB for the imaging test, as shown in Fig. S6 in the Supplemental Material [41]. The raw light field image formed by the microlens array is shown in Fig. S5(d) in the Supplemental Material [41]. The result of wide-field imaging after the rendering process is displayed in Fig. 4(b) in the Supplemental Material [41], where the line width of the upper row letters is 4.17 μm, and that of the bottom row is 2.27 μm. The results show that the microlens array excels in imaging quality in the visible range, with high resolution and exceptional achromatic capability. It achieves this by efficiently focusing on spots near the diffraction limit at different wavelengths through our designed aspherical achromatic sublens. Additionally, our image reconstruction algorithm accurately restores the original object's shape and color.

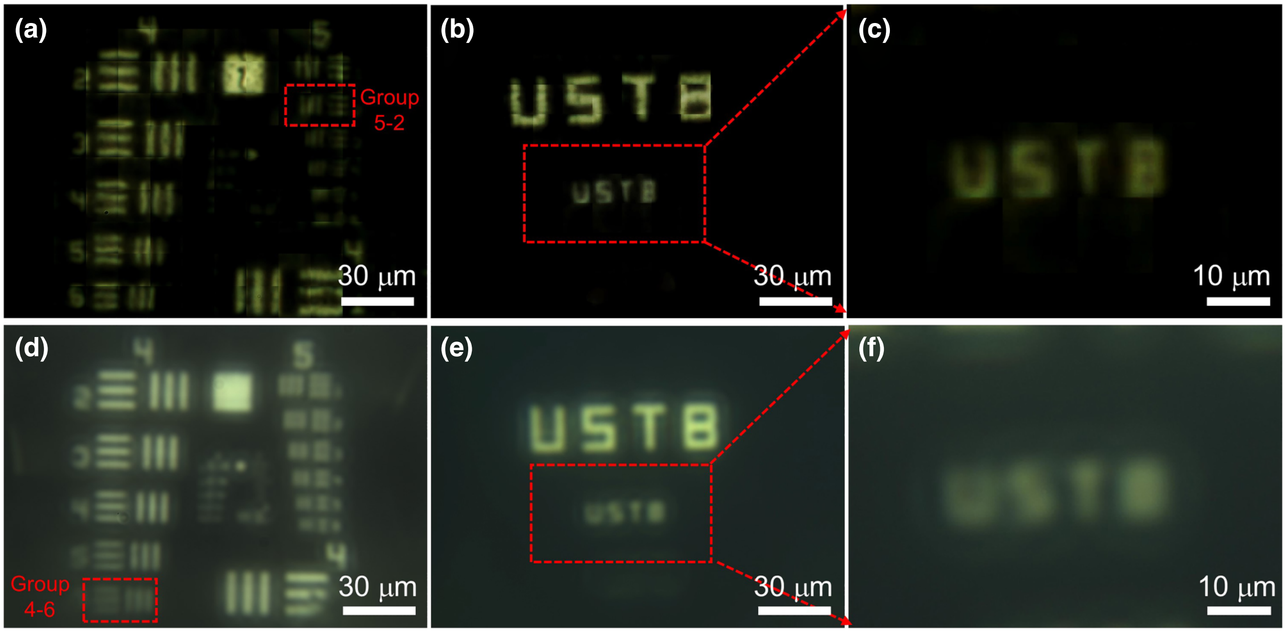

FIG. 4. (a)–(c) Quantitative analysis of imaging resolution of the achromatic microlens array. (a) The rendered image of the 1951 USAF resolution test chart: the smallest distinguishable line is 2.25 μm of group 5-2. (b) The rendered image of fabricated pattern of USTB: the letters' line width of the top row in the image is 4.17 μm and that of the bottom row is 2.27 μm. (c) A magnified view of the regions highlighted with the red dashed line in (b), showing the USTB pattern can be clearly recognized. (d)–(f) Analysis of imaging resolution of the commercial large achromatic lens (NA = 0.161, D = 180 μm, d_0 = 18.37 μm, Ocean Insight Co.) for comparison with a microlens array. (d) The smallest distinguishable line is 3.26 μm of group 6-4. (e) The image of the USTB pattern, showing the letters are significantly blurred. (f) The regions highlighted with the red dashed line in (e) with a larger magnification, showing the letters cannot be recognized.

To evaluate the high-resolution capabilities of the microlens array, we compared it to a commercially available glass achromatic lens (NA = 0.161, Ocean Insight Co.) using the same imaging experimental setup. The commercial lens is a conventional spherical lens, and Fig. S7(a) in the Supplemental Material [41] illustrates the SEM image of the lens. The diameter of the commercial lens is 180 μm, which is close to the effective macroscopic size of the microlens array (180×270 μm^2). The commercial lens's NA of 0.161 is comparable to the that of a sublens of the array (NA = 0.178). The commercial lens has a thickness of 18.37 μm, which is over 16 times thicker than our microlens array (1.12 μm), primarily due to its large spherical lens design.

We imaged the 1951 USAF resolution target and the USTB pattern separately with the commercial lens, and the imaging results are shown in Figs. 4(d) and 4(e). The results illustrate a FOV measuring about 280×200 μm^2, which approximates that of the microlens array (FOV $\sim$ 288×206 μm^2). In the resolution target image captured by the commercial lens, the minimum line width that can be resolved is 3.26 μm in group 4-6. The USTB pattern in the top row can be identified, but there is significant blurring. These images depict the issues encountered with macrosized spherical lenses, including image blurring and distortion of line edges. These observations effectively highlight the limitations and deficiencies of the commercial lens in producing clear and accurate imaging results. To facilitate a more precise assessment of the imaging quality between the microlens array and the commercial lens, we present magnified views in Figs. 4(c) and 4(f). These close-ups clearly demonstrate that our microlenses outperform the commercial lens in the ability to distinguish individual letters and maintain sharp image details. This can be attributed to the presence of spherical aberration in commercial lenses with their spherical shape. The convergence points of on-axis and off-axis rays differ due to the spherical shape, resulting in a diffuse focal spot with a large FWHM. Furthermore, the large diameter leads to an increase in the height of the incident light relative to the center of the lens (the maximum height is approximately equal to the radius of the lens), which results in a larger wave-front aberration [40]. Figure S7(b) in the Supplemental Material [41] provides valuable insights, revealing that the measured FWHM values of the commercial lens are further away from the diffraction limit at all wavelengths. In contrast, our microlens is close to the diffraction limit, as discussed in Fig. 3(c). Our strategy involves arranging small-diameter microlenses to reduce the relative height of incident rays and employing

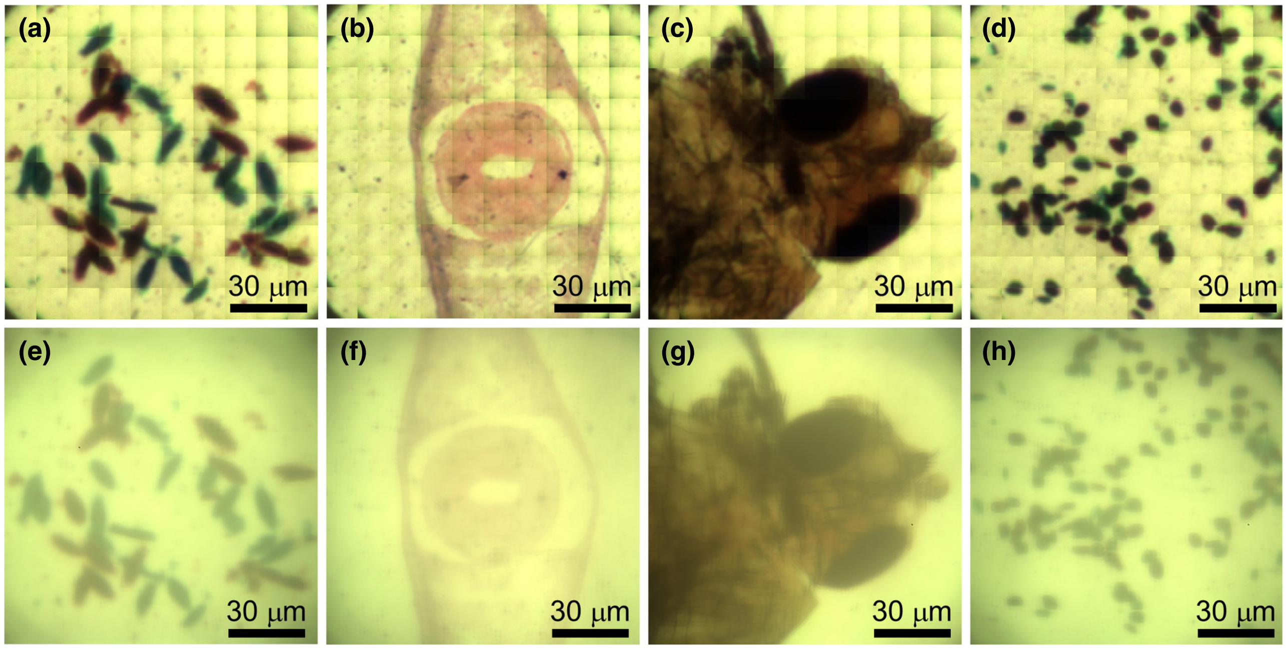

FIG. 5. White-light images of stained parameciums, planaria, fruitfly head, and pollens obtained by (a)–(d) the microlens array and (e)–(h) the commercial lens.

aspherical sublenses. The synergistic effect of these methods enhances resolution while maintaining a wide-FOV comparable to that of commercial lenses. Furthermore, the modulation transfer function (MTF) curves of the two lenses are compared in Figs. S7(c) and S7(d) in the Supplemental Material [41]. It is evident that the MTF curves of our microlens exhibit a more gradual decline across all wavelengths. In quantitative terms, at 10% contrast and a wavelength of 410 nm, our lens achieves a frequency of 377 line pairs (lp)/mm, while the commercial lens reaches only 199 lp/mm. This clear difference in performance substantiates our lens's superior imaging capability in terms of clarity and sharpness. The results unequivocally demonstrate the advantages of using achromatic microlens arrays in expanding the FOV and maintaining image quality, making them an optimal choice for wide-FOV microscopic imaging of biological samples. To validate this, we conducted imaging tests on stained biological samples including parameciums, planaria, fruit fly heads, and pollens.

Figures 5(a)–5(d) showcase the imaging results captured with the microlens array under white light, while Figs. 5(e)–5(h) depict those obtained with the commercial lens. Evidently, the microlens array illustrates the morphology of the biological samples more clearly, showing them in a brighter and higher-contrast manner. This outcome aligns perfectly with the analysis provided, establishing the microlens array's superiority in imaging biological samples with enhanced detail and striking visual quality. In addition, another advantage of microlens arrays lies in their thickness, which is approximately one order of magnitude smaller than that of commercial lenses. Its smaller form factor makes it well suited for integration into miniaturized devices and systems, opening up alternative possibilities for compact and portable optical solutions.

V. CONCLUSIONS

We achieved highly compact and high-resolution widefield imaging by employing a microlens array. Each sublens provides near-diffraction-limited focusing for precise imaging at different positions, providing a high resolution in a wide FOV. With this compact aspheric microlens array design, we address the trade-off between FOV and resolution inherent in conventional large-diameter spherical lenses. The high-resolution wide-field images were obtained with a simple stitching rendering algorithm, and the total image coverage exceeded 150 times that of a single microlens. We systematically studied the imaging performance of the lens array, including resolution, MTF, and FOV. In comparison to a commercially available lens of similar NA and lateral dimensions, our system showed substantial improvement in imaging resolution and reduced lens thickness by an order of magnitude. At the same time, it achieved a comparable FOV, effectively demonstrating the advantages of our microlens array design. This has great applicability in compact optical systems that require wide fields of view and high resolution, such as biological microendoscopy and fluorescence microscopy.

ACKNOWLEDGMENTS

This work was supported by grants from the National Key R&D Program of China (Grant No. 2022YFB3806000), the National Natural Science Foundation of China (Grants No. 52325208, No. 11974203), and the Beijing Municipal Science and Technology Commission (Grant No. Z191100004819002).

[1] M. Khorasaninejad, W. T. Chen, R. C. Devlin, J. Oh, A. Y. Zhu, and F. Capasso, Metalenses at visible wavelengths: Diffraction-limited focusing and subwavelength resolution imaging, Science **352**, 1190 (2016).

[2] R. Wang, M. A. Ansari, H. Ahmed, Y. Li, W. Cai, Y. Liu, S. Li, J. Liu, L. Li, and X. Chen, Compact multi-foci metalens spectrometer, Light: Sci. Appl. **12**, 103 (2023).

[3] P. Zheng, X. Zhang, and H.-C. Liu, Metalens and microtaper spectrometers on a fingertip, Light: Sci. Appl. **12**, 166 (2023).

[4] L. Fan and J. Mei, Flow-permeable and tunable metalens for subdiffraction waterborne-sound focusing, Phys. Rev. Appl. **19**, 024026 (2023).

[5] B. Xu, H. Li, S. Gao, X. Hua, C. Yang, C. Chen, F. Yan, S. Zhu, and T. Li, Metalens-integrated compact imaging devices for wide-field microscopy, Adv. Photonics **2**, 066004 (2020).

[6] X. Luo, F. Zhang, M. Pu, Y. Guo, X. Li, and X. Ma, Recent advances of wide-angle metalenses: Principle, design, and applications, Nanophotonics **11**, 1 (2021).

[7] V. Saragadam, Z. Han, V. Boominathan, L. Huang, S. Tan, J. E. Fröch, K. F. Böhringer, R. G. Baraniuk, A. Majumdar, and A. Veeraraghavan, Foveated thermal computational imaging prototype using all-silicon meta-optics, Optica **11**, 18 (2024).

[8] A. V. Baranikov, E. Khaidarov, E. Lassalle, D. Eschimese, J. Yeo, N. D. Loh, R. Paniagua-Dominguez, and A. I. Kuznetsov, Large field-of-view and multi-color imaging with GaP quadratic metalenses, Laser Photonics Rev. **18**, 2300553 (2024).

[9] F. Zhao, Z. Shen, D. Wang, B. Xu, X. Chen, and Y. Yang, Synthetic aperture metalens, Photonics Res. **9**, 2388 (2021).

[10] M. Pu, X. Li, Y. Guo, X. Ma, and X. Luo, Nanoapertures with ordered rotations: Symmetry transformation and wide-angle flat lensing, Opt. Express **25**, 31471 (2017).

[11] A. Martins, K. Li, J. Li, H. Liang, D. Conteduca, B.-H. V. Borges, T. F. Krauss, and E. R. Martins, On metalenses with arbitrarily wide field of view, ACS Photonics **7**, 2073 (2020).

[12] E. Lassalle, T. W. W. Mass, D. Eschimese, A. V. Baranikov, E. Khaidarov, S. Li, R. Paniagua-Dominguez, and A. I. Kuznetsov, Imaging properties of large field-of-view quadratic metalenses and their applications to fingerprint detection, ACS Photonics **8**, 1457 (2021).

[13] C. Chen, P. Chen, J. Xi, W. Huang, K. Li, L. Liang, F. Shi, and J. Shi, On-chip monolithic wide-angle field-of-view metalens based on quadratic phase profile, AIP Adv. **10**, 115213 (2020).

[14] M. Y. Shalaginov, S. An, F. Yang, P. Su, D. Lyzwa, A. M. Agarwal, H. Zhang, J. Hu, and T. Gu, Single-element diffraction-limited fisheye metalens, Nano Lett. **20**, 7429 (2020).

[15] A. Arbabi, E. Arbabi, S. M. Kamali, Y. Horie, S. Han, and A. Faraon, Miniature optical planar camera based on a wide-angle metasurface doublet corrected for monochromatic aberrations, Nat. Commun. **7**, 13682 (2016).

[16] C. Hao, S. Gao, Q. Ruan, Y. Feng, Y. Li, J. K. W. Yang, Z. Li, and C.-W. Qiu, Single-layer aberration-compensated flat lens for robust wide-angle imaging, Laser Photonics Rev. **14**, 2000017 (2020).

[17] F. Balli, M. Sultan, S. K. Lami, and J. T. Hastings, A hybrid achromatic metalens, Nat. Commun. **11**, 3892 (2020).

[18] A. Li, J. Li, H. Jia, H. Duan, and Y. Hu, The effect of fabrication error on the performance of mid-infrared metalens with large field-of-view, Nanomaterials **13**, 440 (2023).

[19] J. S. Park, S. Zhang, A. She, W. T. Chen, P. Lin, K. M. A. Yousef, J.-X. Cheng, and F. Capasso, All-glass, large metalens at visible wavelength using deep-ultraviolet projection lithography, Nano Lett. **19**, 8673 (2019).

[20] R. Sawant, D. Andren, R. J. Martins, S. Khadir, R. Verre, M. Kall, and P. Genevet, Aberration-corrected large-scale hybrid metalenses, Optica **8**, 1405 (2021).

[21] A. She, S. Zhang, S. Shian, D. R. Clarke, and F. Capasso, Large area metalenses: Design, characterization, and mass manufacturing, Opt. Express **26**, 1573 (2018).

[22] C. A. Dirdal, G. U. Jensen, H. Angelskar, P. Conrad, V. Thrane, J. Gjessing, and D. A. Ordnung, Towards high-throughput large-area metalens fabrication using UV-nanoimprint lithography and Bosch deep reactive ion etching, Opt. Express **28**, 15542 (2020).

[23] J. Chen, X. Ye, S. Gao, Y. Chen, Y. Zhao, C. Huang, K. Qiu, S. Zhu, and T. Li, Planar wide-angle-imaging camera enabled by metalens array, Optica **9**, 431 (2022).

[24] J. Hu and W. Yang, Metalens array miniaturized microscope for large-field-of-view imaging, Opt. Commun. **555**, 130231 (2024).

[25] R. J. Lin, V. C. Su, S. Wang, M. K. Chen, T. L. Chung, Y. H. Chen, H. Y. Kuo, J. W. Chen, J. Chen, Y. T. Huang, *et al.*, Achromatic metalens array for full-colour light-field imaging, Nat. Nanotechnol. **14**, 227 (2019).

[26] X. Hua, Y. J. Wang, S. M. Wang, X. J. Zou, Y. Zhou, L. Li, F. Yan, X. Cao, S. M. Xiao, D. P. Tsai, *et al.*, Ultra-compact snapshot spectral light-field imaging, Nat. Commun. **13**, 2732 (2022).

[27] Z. B. Fan, H. Y. Qiu, H. L. Zhang, X. N. Pang, L. D. Zhou, L. Liu, H. Ren, Q. H. Wang, and J. W. Dong, A broadband achromatic metalens array for integral imaging in the visible, Light: Sci. Appl. **8**, 67 (2019).

[28] F. capasso, Compact single-shot metalens depth sensors inspired, Proc. Natl. Acad. Sci. U. S. A. **116**, 22959 (2019).

[29] R. C. Devlin, M. Khorasaninejad, W. T. Chen, J. Oh, and F. Capasso, Broadband high-efficiency dielectric metasurfaces for the visible spectrum, Proc. Natl. Acad. Sci. U. S. A. **113**, 10473 (2016).

[30] B. Xiong, J. N. Wang, R. W. Peng, H. Jing, R. H. Fan, D. X. Qi, F. Chen, and M. Wang, Construct achromatic polymer microlens for high-transmission full-color imaging, Adv. Opt. Mater. **9**, 2001524 (2020).

[31] S. Surdo, R. Carzino, A. Diaspro, and M. Duocastella, Single-shot laser additive manufacturing of high fill-factor microlens arrays, Adv. Opt. Mater. **6**, 1701190 (2018).

[32] M. Zohrabi, W. Y. Lim, S. Gilinsky, V. M. Bright, and J. T. Gopinath, Adaptive aberration correction using an electrowetting array, Appl. Phys. Lett. **122**, 081102 (2023).

[33] C. Fang, J. Zheng, Y. Zhang, Y. Li, S. Liu, W. Wang, T. Jiang, X. Zhao, and Z. Li, Antireflective paraboloidal microlens film for boosting power conversion efficiency of solar cells, ACS Appl. Mater. Interfaces **10**, 21950 (2018).

[34] C. Yuan, K. Kowsari, S. Panjwani, Z. Chen, D. Wang, B. Zhang, C. J.-X. Ng, P. V. y. Alvarado, and Q. Ge, Ultrafast three-dimensional printing of optically smooth microlens arrays by oscillation-assisted digital light processing, ACS Appl. Mater. Interfaces **11**, 40662 (2019).

[35] Y. Wei, Q. Yang, H. Bian, F. Chen, M. Li, Y. Dai, and X. Hou, Fabrication of high integrated microlens arrays on a glass substrate for 3D micro-optical systems, Appl. Surf. Sci. **457**, 1202 (2018).

[36] X. Wang, F. Wang, C. Liu, W. Luo, C. Tao, Y. Hou, L. Qiao, J. Zhou, J. Sun, and Y. Bai, Highly efficient broadband achromatic microlens design based on low dispersion materials, Engineering accepted.

[37] M. Khorasaninejad, Z. Shi, A. Y. Zhu, W. T. Chen, V. Sanjeev, A. Zaidi, and F. Capasso, Achromatic metalens over 60 nm bandwidth in the visible and metalens with reverse chromatic dispersion, Nano Lett. **17**, 1819 (2016).

[38] A. Arbabi, Y. Horie, A. J. Ball, M. Bagheri, and A. Faraon, Subwavelength-thick lenses with high numerical apertures and large efficiency based on high-contrast transmitarrays, Nat. Commun. **6**, 7069 (2015).

[39] S. Shrestha, A. C. Overvig, M. Lu, A. Stein, and N. Yu, Broadband achromatic dielectric metalenses, Light: Sci. Appl. **7**, 85 (2018).

[40] G. R. Brady, McGill University (Canada), (2000).

[41] See the Supplemental Material at http://link.aps.org/supplemental/10.1103/PhysRevApplied.21.034035 for the details of the numerical simulation of the microlens, the preparation process of microlens arrays, analysis of the effect of microlens fabrication errors, schematic diagram of the experimental setup, imaging performance of the microlens array, and measured optical performance of commercial glass spherical lens.